Nano Research
2019, 12(12): 2933–2940
ISSN 1998-0124 CN 11-5974/O4
https://doi.org/10.1007/s12274-019-2527-0

Research Article

Resolution and contrast enhancement of laser-scanning multiphoton microscopy using thulium-doped upconversion nanoparticles

Alexey B. Kostyuk[1], Artem D. Vorotnov[1], Andrey V. Ivanov[2], Arthur B. Volovetskiy[1], Aleksandr V. Kruglov[1], Lyudmila M. Sencha[1], Liuen Liang[3], Evgenii L. Guryev[1], Vladimir A. Vodeneev[1], Sergey M. Deyev[4], Yiqing Lu[3], and Andrei V. Zvyagin[1,2,3] (✉)

[1] *Lobachevsky State University of Nizhny Novgorod, Nizhny Novgorod 603950, Russia*
[2] *Center of Biomedical Engineering, Institute of Molecular Medicine, Sechenov University, Moscow 119991, Russia*
[3] *ARC Centre of Excellence "Nanoscale BioPhotonics", Department of Physics and Astronomy, Macquarie University, Sydney 2109, Australia*
[4] *Institute of Bioorganic Chemistry, Russian Academy of Sciences, Moscow 117997, Russia*

Received: 29 June 2019 / **Revised:** 26 September 2019 / **Accepted:** 27 September 2019

ABSTRACT

High-contrast optical imaging is achievable using phosphorescent labels to suppress the short-lived background due to the optical backscatter and autofluorescence. However, the long-lived phosphorescence is generally incompatible with high-speed laser-scanning imaging modalities. Here, we show that upconversion nanoparticles of structure $NaYF_4$:Yb co-doped with 8% Tm (8T-UCNP) in combination with a commercial laser-scanning multiphoton microscopy are uniquely suited for labeling biological systems to acquire high-resolution images with the enhanced contrast. In comparison with many phosphorescent labels, the 8T-UCNP emission lifetime of ~ 15 μs affords rapid image acquisition. The high-order optical nonlinearity of the 8T-UCNP ($n \approx 4$, as confirmed experimentally and theoretically) afforded pushing the resolution limit attainable with UCNPs to the diffraction-limit. The contrast enhancement was achieved by suppressing the background using (i) bandpass spectral filtering of the narrow emission peak of 8T-UCNP at 455-nm, and (ii) time-gating implemented with a time-correlated single-photon counting system that demonstrated the contrast enhancement of > 2.5-fold of polyethyleneimine-coated 8T-UCNPs taken up by human breast adenocarcinoma cells SK-BR-3. As a result, discrete 8T-UCNP nanoparticles became clearly observable in the freshly excised spleen tissue of laboratory mice 15-min post intravenous injection of an 8T-UCNP solution. The demonstrated approach paves the way for high-contrast, high-resolution, and high-speed multiphoton microscopy in challenging environments of intense autofluorescence, exogenous staining, and turbidity, as typically occur in intravital imaging.

KEYWORDS

upconversion nanoparticles, autofluorescence, time-gated imaging, scanning microscopy, time-correlated single photon counting

1 Introduction

Over the past two decades, laser-scanning multiphoton microscopy (MPM) has become a powerful tool for morphological and functional imaging of cells, tissues, and live animals at the sub-micron resolution [1–4]. In a typical MPM setting, the sample excitation takes place in the near-infrared (NIR) spectral range termed biological tissue transparency window [5] while emission is detected in the ultraviolet (UV) [6], visible, and NIR ranges [7]. The advantages of MPM include enhanced penetration of the NIR excitation into biological tissues (~ 200 μm) [8], reduced autofluorescence background limited by the scanning plane [9], and the reduced phototoxicity of the excitation light [2].

Among a large variety of the excitation mechanisms of MPM, two- and three-photon excited fluorescence, second and third harmonic generation [10–13] and upconversion (UC) processes [7, 14] rely on the conversion of two or more lower-energy photons to a high-energy photon. The signal power P_{em} and excitation intensity I_{ex} of these processes relate to each other by the following equation:

$$P_{em} \sim I_{ex}^{n} \quad (1)$$

where n stands for the number of absorbed photons. The UC process stands alone, as it relies on the successive absorption of several NIR photons via real energy levels, and typically requires much lower excitation intensities (I_{ex} ~ 10–100 W/cm^2) in comparison with $I_{ex} \sim 10^6$ W/cm^2 used in the other MPM modalities. The UC process obeys the rule expressed in Eq. (1), with $n \approx 2$ for the most cases of two-photon processes [15] but n can reach the higher values for the higher-order UC processes ($n \approx 4$ and 5) [16, 17]. Since the five-photon UC process produces UV emission, it poses practical limitations for biomedical imaging due to the high absorption of the UV radiation by conventional microscope optics and high scattering/absorption of the UV radiation by biological systems (albeit the UV-generated phototoxicity can be beneficial for photodynamic therapy [18]). It has been realized that the higher degree of the optical process non-linearity results in the higher spatial resolution [19]. Therefore, the four-photon UC excitation of the emerging nanomaterial —upconversion nanoparticles (UCNPs)—is expected to provide the higher spatial resolution compared with that provided by the other MPM processes typically characterized by $n = 2$ or 3.

Alongside the potential for the improved spatial resolution, UCNPs have several unique properties that complement the MPM merits.

Address correspondence to andrei.zvyagin@mq.edu.au

The UCNP excitation can be realized by means of a low-cost continuous-wave laser operating at approximately 975 nm, or by a femtosecond (fs) laser integrated into an MPM system and tuned to 975 nm. A fast laser-scanning microscopy illuminated with a cw laser diode at 980 nm with a dwell time of 10 μs per pixel has been demonstrated for stimulated emission depletion imaging [20]. The UCNP excitation in the NIR by a continuous-wave laser leads to a negligibly small fluorescent response of the biological tissue (autofluorescence) [21] that significantly increases the UCNP contrast against the autofluorescence background [22]. In comparison with widespread fluorescent organic dyes and fluorescent proteins, UCNP is chemically inert [23] and photostable [24], and its emission is characterized by narrow photoluminescence (PL) bands with a significant anti-Stokes spectral shift relative to the excitation wavelength to enable efficient and affordable spectral filtering [25]. UCNP's mild or no cytotoxicity has been reported [26], and polymer-coated UCNPs found biocompatible [27]. The relatively long PL emission lifetime (τ_{UC} = 100 μs–10 ms) of UCNPs and other phosphorescent materials [28] enables applying time-delayed PL detection schemes to suppress the autofluorescence background characterized by short-lived fluorescence [29]. The time-gating schemes are conventionally and conveniently implemented in wide-field microscopy and imaging configuration [30], with a few notable exceptions [31]. However, the required excitation intensity for UCNPs [32] and some phosphorescent materials [31] is not always possible to achieve in wide-field microscopy, as it is achievable in a laser-scanning MPM modality. Unfortunately, the employment of UCNPs for labeling biological specimens in laser-scanning MPM is limited due to the long τ_{UC}. The dwell time of the excitation laser beam per pixel must be $t_{dw} > \tau_{UC}$ (optimally, $t_{dw} = 5\tau_{UC}$) to ensure lossless collection of the PL emission. This results in an impractically long image acquisition time, reportedly, 30 min per image [33]. The high scanning rate ($t_{dw} < \tau_{UC}$) can also lead to image blurring along the fast scanning axis [21].

It was recently shown that τ_{UC} of the structure can be controlled in UCNP by varying the concentration of dopant lanthanide ions, which function as sensitizers and activators [29, 34–36].

In this paper, we demonstrate that UCNPs of structure $NaYF_4$:Yb heavily co-doped with 8% Tm (8T-UCNP) [16, 37] in combination with a commercial laser-scanning multiphoton microscopy are uniquely suited for labeling biological systems to acquire high-resolution enhanced-contrast images. The high resolution was achieved due to the high degree of optical nonlinearity of 8T-UCNP (n = 4) in which the four-photon process populated the energy level $^1D_2$ of Tm, followed by the radiative transition ($^1D_2 \rightarrow {}^3F_4$) at 455 nm. The contrast enhancement was achieved by bandpass spectral filtering of the narrow emission peak of 8T-UCNP at 455-nm. We further employed time-correlated single photon counting synchronized with the fs-laser excitation to suppress the background, which allowed truncation of the acquired time window to exclude the unwanted signals from fast-decaying autofluorescence and optical backscatter. As a result, the long-lived emission from UCNPs becomes the main contributor to the detected signal leading to a contrast enhancement in cells (> 2.5-fold) as well as in animal tissues (> 3.5-fold). In comparison with many phosphorescent labels, the 8T-UCNP emission lifetime of ~ 15 μs affords rapid image acquisition.

2 Experimental

2.1 8T-UCNP sample preparation and characterization

UCNPs $NaYF_4$ in a hexagonal β-phase codoped with 20 mol% Yb^{3+} and 8 mol% Tm^{3+} were synthesized using a solvothermal decomposition method described in detail elsewhere [36]. The 8T-UCNP surface was polymer-coated with polyethyleneimine (PEI) to endow the nanoparticles colloidal stability in aqueous solutions. To modify 8T-UCNPs with PEI, nitrosonium tetrafluoroborate ($NOBF_4$) was used to displace oleate groups on the 8T-UCNP surface with PEI via a ligand exchange reaction. Typically, 5-mL N,N-dimethylformamide (DMF) solution of $NOBF_4$ (0.01 M) was mixed with 5 mL of the 8T-UCNP cyclohexane solution (5 mg/mL), and the solution mixture was stirred overnight at room temperature. Then, the 8T-UCNPs were centrifuged, redispersed with DMF, and flocculated with a toluene and cyclohexane mixture (1:1 w/w). Next, the 8T-UCNPs were washed twice with ethanol and were dispersed in 5 mL of ethanol. 100 mg of PEI was also dissolved in 5 mL of ethanol and was mixed with the 8T-UCNP ethanol solution under vigorous stirring at room temperature for 24 h. Finally, the unbound PEI molecules were removed by centrifugation, and the nanoparticles were washed with ethanol and twice with distilled water. Further, 8T-UCNP-PEIs were stored in distilled water.

8T-UCNP nanoparticles were characterized by transmission electron microscopy (TEM), dynamic light scattering (DLS), and laser Doppler velocimetry (LDV). TEM images of the prepared samples were obtained using a Philips CM10 transmission electron microscope operating at 100 kV. For a TEM specimen preparation, a 5-μL drop of 8T-UCNP in cyclohexane or 8T-UCNP-PEI water dispersion was deposited on a carbon-coated Cu grid and dried under ambient conditions.

DLS and LDV measurements were carried out using a Zetasizer Nano ZS (Malvern Panalytical, UK) with a 633-nm He-Ne laser at 25 °C. DLS data sets were taken at least in five copies using a polystyrene cuvette (Sarstedt AG & Co. KG, Germany) and analyzed using the number distributions. LDV measurements were carried out in a disposable folded capillary zeta-potential cell (Malvern Panalytical, UK).

2.2 Optical measurements

The experimental setup used for the optical measurements of 8T-UCNPs is schematically shown in Fig. 1. A simplified optical-path scheme for three image acquisition modes and PL decay acquisition mode are also shown. Samples were excited by a mode-locked Ti:Sa laser Chameleon Vision II (Coherent, USA) tuned to the 975-nm

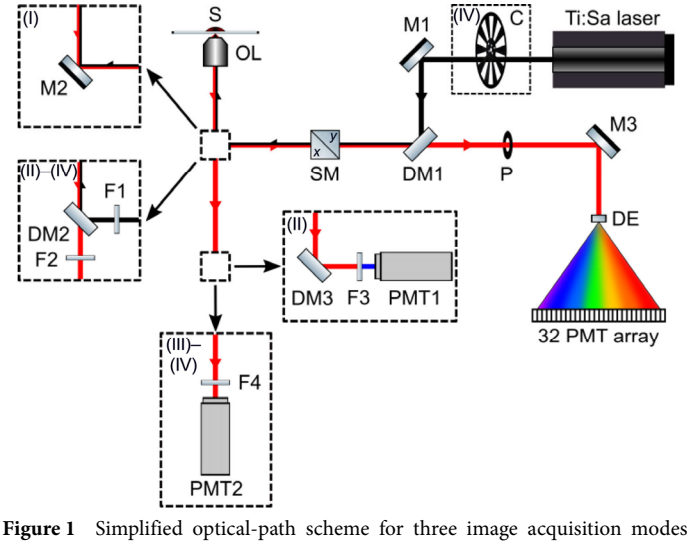

Figure 1 Simplified optical-path scheme for three image acquisition modes and PL decay acquisition mode: (I) Lambda mode, (II) high-resolution mode, (III) high-contrast mode, and (IV) PL decay acquisition mode. C stands for chopper; DM1—short-pass dichroic mirror, cutoff 760 nm; SM—scanning module; OL—objective lens; S—sample, P—pinhole, DE—dispersive element; F1—long-pass edge filter, cutoff 846 nm; DM2—short-pass dichroic mirror, cutoff 950 nm; F2—edge short-pass emission filter, cutoff 860 nm; DM3—long-pass dichroic mirror, cutoff 552-nm; F3—bandpass filter, bandwidth, 446-486 nm; PMT1—photomultiplier of NDD module; F4—edge short-pass emission filter, cutoff 831-nm; PMT2—hybrid photodetector HPM-100-40; and M1, M2, and M3—sliver-coated reflection mirrors.

center wavelength with a repetition rate of 80 MHz and a pulse duration of ~ 100 fs. Laser radiation was introduced into an Axio Observer Z1 LSM 710 DUO NLO laser-scanning microscope (Carl Zeiss, Germany).

Mode (I): PL spectra of a 8T-UCNP-PEI aqueous solution and spectral images of cells and tissues labelled with 8T-UCNP-PEI were obtained using Lambda mode. The laser radiation was coupled to the rear port of the microscope and reflected from a dichroic beam splitter MBS 760+ (DM1) towards the sample, passed through a scanning module (SM), reflected from a mirror (M2) and focused on the sample by using an oil-immersion objective lens (OL) NA 1.4 (C Plan-Apochromat 63×/1.4 Oil DIC Carl Zeiss, Germany) with a high magnification of 63×. PL of samples was collected with the same OL, reflected from M2, and passed through a SM, DM1, fully opened P, and a DE in the direction of 32 PMT arrays, where it was recorded in a wide spectral range of 425–725 nm.

Mode (II): To image 8T-UCNP-PEI-labelled samples in a high-resolution mode, radiation from the Ti:Sa laser also passed through the back port of the microscope, was reflected from the DM1 and passed through a SM and long-pass edge filter (F1) (BLP01-830R, Semrock, USA) transmitting the laser radiation. Then, instead of the mirror used in the Lambda mode, it was reflected from a dichroic mirror (DM2) (ZT1064rdc-sp, Chroma, USA) towards the sample. PL was collected by the same lens, passed through DM2 and an edge short-pass emission filter (F2) (FF01-890/SP, Semrock, USA) blocking the laser radiation. Next, PL signal was passed through a side non-descanned detection (NDD) port of the microscope towards a photodetector (PMT1) by reflecting from a dichroic beam splitter (DM3) (FF552-Di02, Semrock, USA) and passing through a bandpass filter (F3) (FF01-466/40, Semrock, USA), with a narrow band of 446–486 nm.

Mode (III): For imaging of 8T-UCNP-PEI-labelled samples in a high-contrast mode, the optical path of the exciting radiation from the laser to the sample and PL from the sample to the NDD port was identical to that of the high-resolution mode. The NDD port was connected to a time-correlated single photon counting (TCSPC) system (Simple-Tau 152, Becker & Hickl GmbH, Germany) with an edge short-pass emission filter (F4) (FF01-842/SP, Semrock, USA) installed. A hybrid photodetector (PMT2) HPM-100-40 (Becker & Hickl GmbH, Germany) was used for the photoelectric conversion of PL emission ranged from 440–831 nm. The acquired signal was processed by a SPC-150 card (Becker&Hickl GmbH, Germany) synchronized to a laser pulse to count the arrival time of photons.

The collected time-resolved data were further analyzed with SPCImage software (Becker & Hickl GmbH, Germany). Short-lived and long-lived components of the fluorescence image were obtained by integrating the measured photon histogram of each pixel over the respective time windows.

Mode (IV): To obtain the PL decay acquisition for 8T-UCNP-PEI particles deposited on a coverslip, the same optical path scheme was used as for imaging 8T-UCNP-PEI in the high-contrast mode. In this case, using SM, the laser radiation was sequentially focused to the location of 8T-UCNP-PEI particles on the coverslip. In addition, to record the kinetics of PL, the laser radiation was interrupted using an optical chopper (C) MC2000B (Thorlabs, USA) synchronized with the TCSPC system. The chopper speed was set to 1 kHz. Analysis of the PL decay curves for 8T-UCNP-PEIs was carried out using the SPCImage software.

The average power of the Ti:Sa laser was measured using a PM100A power meter (ThorLabs Inc., USA) equipped with a S121C standard photodiode power sensor (Thorlabs, USA).

2.3 High-contrast imaging of 8T-UCNP-PEIs in cells and tissues

8T-UCNP-PEIs were incubated with human breast adenocarcinoma cells (SK-BR-3, no. ATCC HTB-30) to demonstrate imaging of discrete 8T-UCNP-PEIs by using the proposed PL detection scheme in mode (III). Initially, SK-BR-3 cells were pre-plated on 96-well plates (BD Falcon, USA) in the amount of 1×10^4 cells per well and cultured over 24 h in an incubator at 37 °C in an atmosphere of 5% CO_2. To minimize or eliminate protein-corona mediated aggregation of 8T-UCNP-PEIs, the culture medium was replaced with a colloidal solution of 8T-UCNP-PEI-s in phosphate buffered saline (PBS) at the concentration of 10 μg/mL and incubated in a CO_2-atmosphere for 2 h. After incubation, the 8T-UCNP-PEI solution in plate wells was replaced with a standard growth medium (DMEM) supplemented with 10% fetal bovine serum and left overnight in the CO_2-incubator. Then, the cells were fixed by adding 4% formaldehyde. To establish the PL signal level of a discrete 8T-UCNP-PEI, the PL intensity distribution of individual 8T-UCNP-PEIs were acquired by the MPM and matched to the corresponding images acquired by atomic force microscopy (AFM), scanning probe microscope Solver Pro-M (NT-MDT, Russia).

High-contrast images of 8T-UCNP-PEIs on tissue sections of laboratory mice were also acquired. 200-μg/mL 8T-UCNP-PEIs formulated in 150-μL PBS were injected into the tail vein of a Balb/c mouse (females, 10-wk age, 18–22 g) pro-cured from the laboratory animal nursery of the Institute of Biological Sciences, Russian Academy of Sciences (Push-chino). The treated animals were sacrificed 15 min post-injection by dislocation of the cervical vertebrae, and organs, including the spleen, were harvested, tissue-sectioned and imaged straight away, without fixation or freezing. Longitudinal sections of the spleen were cut in the depth of the organ, and the sections were placed on the cover slip.

All experiments with animal were approved by the Bioethics Committee at the State University of Nizhny Novgorod. Experiments were performed in strict accordance with Act 708n (23.08.2010) of the National Ministry of Public Health of the Russian Federation approving the rules of laboratory practice for the care and use of laboratory animals and Council Directive 2010/63EU of the European Parliament (September 22, 2010) on the protection of animals used for scientific purposes.

2.4 Kinetic modeling of amplified stimulated emission of 8T-UCNP

To simulate the 8T-UCNP emission at 455 nm resulted from the four-photon excitation by a 975-nm laser, we used a kinetic approach described elsewhere [38–40]. The 455-nm emission occurs via a transition $^1D_2 \rightarrow {}^3F_4$, as shown in a simplified energy level diagram in Fig. 2. Note that the femtosecond and continuous-wave laser

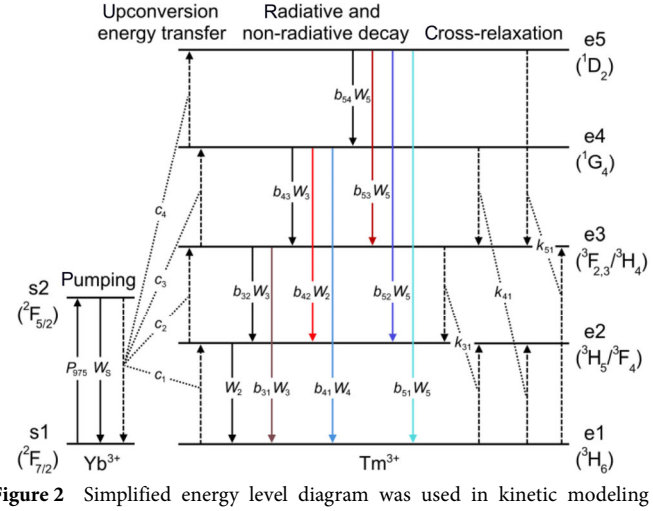

Figure 2 Simplified energy level diagram was used in kinetic modeling of 8T-UCNP emission upon excitation by a 975-nm laser (adapted with permission from Ref. [16], © Spring Nature 2017).

excitations at 975 nm were equivalent provided the averaged power is equal. We schematize the energy levels of a sensitizer Yb^{3+} as two levels $^2F_{7/2}$ and $^2F_{5/2}$ denoted as s1 and s2, respectively, and the energy levels of an activator Tm^{3+} as five energy levels $^3H_6$, $^3H_5/^3F_4$, $^3F_{2,3}/^3H_4$, $^1G_4$, and $^1D_2$ denoted as e1, e2, e3, e4, and e5, respectively. We assume that the laser excitation is absorbed by the sensitizer, energy transfer UC occurs between the sensitizer at the excited level s2 and the activator at the e1, e2, e3, and e4 levels, and cross-relaxation occurs in the activator at both the ground e1 and excited e3, e4, and e5 levels while the other non-radiative relaxation pathways are ignored.

A system of nonlinear differential equations used in the kinetic modeling is given as follows

$$\begin{aligned}
\frac{dn_{s2}}{dt} &= P_{975}n_{s1} - W_s n_{s2} - (c_1 n_{e1} + c_2 n_{e2} + c_3 n_{e3} + c_4 n_{e4})n_{s2} \\
\frac{dn_{e2}}{dt} &= c_1 n_{s2} n_{e1} - c_2 n_{s2} n_{e2} - W_2 n_{e2} + b_{32} W_3 n_{e3} + b_{42} W_4 n_{e4} \\
&\quad + b_{52} W_5 n_{e5} + 2k_{31} n_{e1} n_{e3} + k_{41} n_{e1} n_{e4} \\
\frac{dn_{e3}}{dt} &= c_2 n_{s2} n_{e2} - c_3 n_{s2} n_{e3} - W_3 n_{e3} + b_{43} W_4 n_{e4} + b_{53} W_5 n_{e5} - k_{31} n_{e1} n_{e3} \\
&\quad + k_{41} n_{e1} n_{e4} + 2k_{51} n_{e1} n_{e5} \\
\frac{dn_{e4}}{dt} &= c_3 n_{s2} n_{e3} - c_4 n_{s2} n_{e4} - W_4 n_{e4} + b_{54} W_5 n_{e5} - k_{41} n_{e1} n_{e4} \\
\frac{dn_{e5}}{dt} &= c_4 n_{s2} n_{e4} - W_5 n_{e5} + k_{51} n_{e1} n_{e5}
\end{aligned} \quad (2)$$

where P_{975} is the absorption rate of Yb^{3+} ($P_{975} = \sigma_{975}\lambda_{975}I_{975}/hc$, where λ_{975} is the excitation wavelength 975 nm, I_{975} is the excitation intensity at λ_{975}, σ_{975} is the absorption cross-section of Yb^{3+} at λ_{975}, h is the Planck constant, and c is the speed of light), W_s is intrinsic decay rate of excited Yb^{3+}; c_i is the UC coefficient between the excited Yb^{3+} and Tm^{3+} on the level i; W_i is the intrinsic decay rate of Tm^{3+} of the level i; b_{ij} is the branching ratio for Tm^{3+} decaying from the level i to level j satisfying $\sum_{j=1}^{i-1} b_{ij} = 1$; k_{ij} is the cross-relaxation coefficient of Tm^{3+} between the levels i and j; and n_i is relative population of ions on the energy level i satisfying

$$n_{s1} + n_{s2} = 1 \text{ and } n_{e1} + n_{e2} + n_{e3} + n_{e4} + n_{e5} = 1 \quad (3)$$

The initial conditions are specified as follows

$$n_{s1} = 1,\ n_{s2} = 0,\ n_{e1} = 1,\ n_{e2} = n_{e3} = n_{e4} = n_{e5} = 0 \text{ and } P_{975} = 9 \times 10^4 \text{ ph/s} \quad (4)$$

This set of kinetic equations is solved numerically by using Mathematica. The rate constants used in Eqs. (2)–(4) are extracted by fitting experimental data on the transient responses and the absorption rate dependence of a PL signal at 455 nm. Then, the parameterized model is applied to describe kinetic behavior of 8T-UCNP emission under experimental conditions.

3 Results and discussion

3.1 8T-UCNP Characterization

As-synthesized 8T-UCNP particles were imaged by using TEM (see Fig. 1(a)). The size distribution of this sample was found to be monodisperse with a mean nanocrystal diameter of 21.7 ± 0.2 nm, as shown in Fig. 3(b).

Figure 3(c) presents the DLS results showing that the average hydrodynamic size of nanoparticles after the surface-coating with PEI was slightly increased to 25.0 ± 1.5 nm due to a ~ 2-nm-thick PEI layer, as shown in the inset of Fig. 3(c). The zeta potential of 8T-UCNP-PEIs in aqueous solution (pH 5.0) was measured to be 56.5 ± 1.1 mV due the positively charged PEI layer, which improved

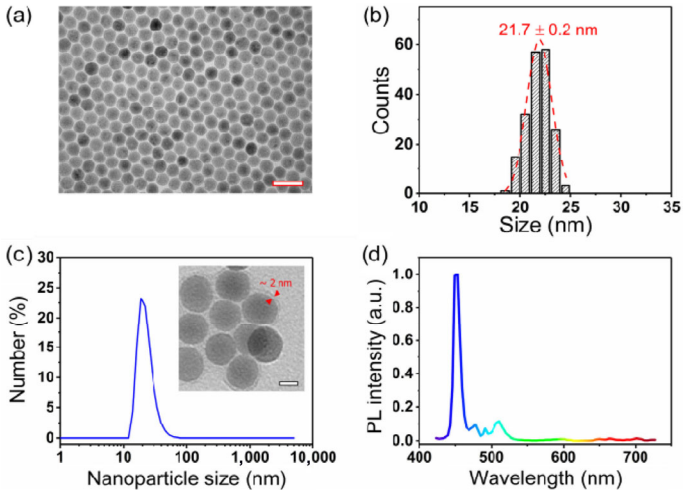

Figure 3 (a) TEM image of 8T-UCNP nanocrystals and (b) particle size distribution. Scale bar, 50 nm. Gaussian fitting is shown by red dash line. (c) DLS size distribution of 8T-UCNP-PEIs in water. Inset: TEM image of 8T-UCNP-PEI nanocrystals. Scale bar, 10 nm. Red arrows show 2-nm thick PEI layer. (d) PL spectrum of 8T-UCNP-PEIs in water.

colloidal stability of 8T-UCNP-PEIs. PEI surface coating is generally known as cytotoxic. At the same time, it is superior for colloidal stability of UCNPs and preserving their photoluminescent properties. We addressed this trade off by applying additional polymer coating on PEI-precoated UCNPs as reported in Ref. [41].

Figure 3(d) shows PL spectrum of 8T-UCNP-PEIs in aqueous solution obtained in the Lambda mode. The emission spectrum was distinct by intense peaks at 455, 480, and 514 nm corresponding to the $^1D_2 \rightarrow {}^3F_4$, $^1G_4 \rightarrow {}^3H_6$, and $^1D_2 \rightarrow {}^3H_5$ transitions in Tm^{3+}, with the 455-nm peak being the most intense.

3.2 Modeling results and comparison with experimental data

The developed kinetic model was applied to fit the experimental data. 8T-UCNP emission at 455-nm was measured and fitted using the kinetic model, as shown in Fig. 4(a). The obtained rate parameters showed that the cross-relaxation rates were much greater than the PL decay rates from the higher excited levels to the ground level. This finding was not surprising due to the strong cooperation in 8T-UCNP in the presence of the 975-nm laser excitation. The heavy Tm^{3+}-doping of 8% resulted in the concentration of ~ 1.2 ion/nm^3 to confine the emitting ions to a volume $\ll \lambda_{455}$ [42]. This strong ion coalescence resulted in fast cross-relaxation leading to a photon avalanche [16]. The S-shape curve over the build-up period (Fig. 4(a)) represented a signature of the photon avalanche effect.

The parameterized model was used to determine the τ_{UC} lifetime of the excited 8T-UCNP by fitting the experimental results of PL decay measurements, τ_{UC} = 14.5 ± 0.7 μs. τ_{UC} was short enough to set the pixel dwell time t_{dw} to 177 μs (see Section 3.4 for details) to ensure adequate sampling of the PL signal in the mode (III).

Figure 4(c) presents the calculated absorption rate dependence of relative population of the highest e5 ($^1D_2$, Tm^{3+}) level and compares it with the corresponding experimental data (the normalized 455-nm PL signal of 8T-UCNP-PEI excited at 975 nm). The results of the modeling are in excellent agreement with the experimental data.

3.3 High-resolution 8T-UCNP imaging

The fourth order nonlinear optical absorption of 8T-UCNP-PEI results in the improved spatial resolution in laser-scanning MPM, with full width at half maximum (FWHM) of a diffraction spot expressed by the following formula [19]

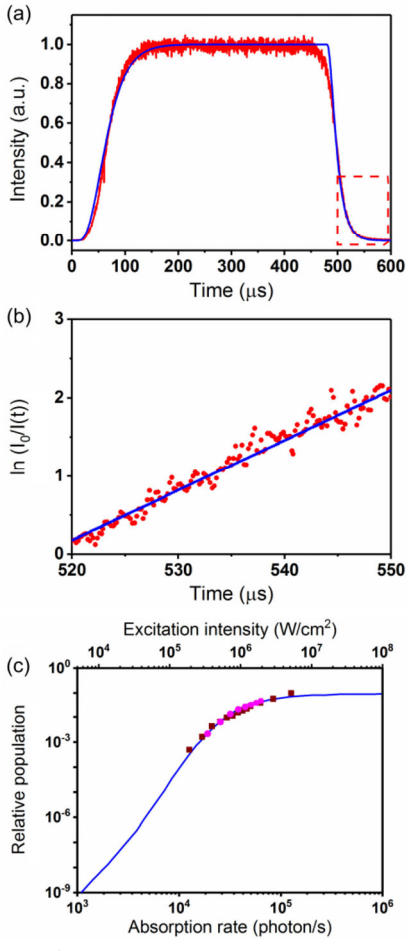

Figure 4 Modeling of 8T-UCNP emission. (a) Transient response of 8T-UCNP emission at 455 nm (red) to a rectangular excitation pulse at 975 nm (not shown) using the kinetic model fitting (blue), (b) A PL decay extracted from (a) (red dashed rectangle) and reploted in a semi-logarithmic scale to emphasize a mono-exponential decay fitted (blue) with the exponent factor τ_{UC} = 14.5 ± 0.7 μs. (c) Plot of the calculated radiative relative population level $^1D_2$ of Tm^{3+} (blue) and measured 8T-UCNP-PEI PL relative signal intensity at 455 nm (brown and magenta squares) versus the photon absorption rate rescaled as the excitation at 975 nm.

$$\mathrm{FWHM}_n = \frac{0.51\lambda_{ex}}{\mathrm{NA}\sqrt{n}} \quad (5)$$

where λ_{ex} is the excitation wavelength, and NA is the objective numerical aperture. FWHM_4 is calculated to be 178 nm at NA = 1.4 and λ_{ex} = 975 nm.

Considering the nonlinearity order (n) variation versus the excitation intensity (c.f. Fig. 4(c)), the FWHM_n dependence of discrete 8T-UCNP-PEIs deposited on a coverslip versus I_{ex} (presented in terms of the excitation power, P_{ex}, labeled as average power) was measured and plotted in Fig. 5, alongside epiluminescent images of discrete 8T-UCNP-PEIs on a coverslip obtained at the corresponding excitation powers. FWHM_4 was measured to be 217 ± 5 nm at P_{ex}= 0.53 mW, comparable with the calculated diffraction-limited FWHM_4 of 8T-UCNP-PEI. We note that the objective lens was not corrected for 975 nm, so that the diffraction limit was not fully achieved in the experiment due to considerable aberrations.

3.4 High-contrast 8T-UCNP imaging in cells and tissues

8T-UCNP-PEI PL was acquired in a broad spectral range of 440–831 nm to maximize emitted photon collection. In the context of biological imaging, the femtosecond laser excited endogenous fluorochromes (see Fig. 6) with the emission spectrum overlapping that of 8T-UCNP-PEIs.

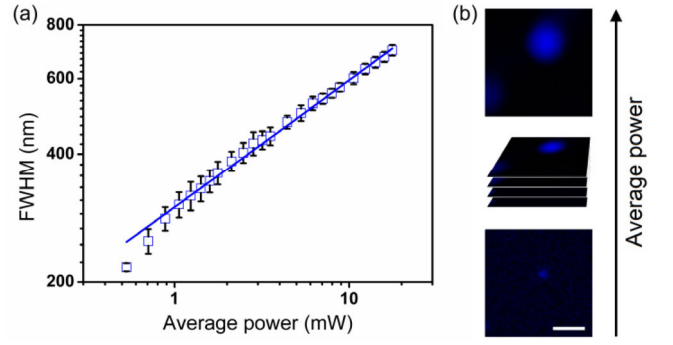

Figure 5 (a) Plot of FWHM of 8T-UCNP-PEI diffraction spots versus the excitation power P_{ex} at 975 nm. Squares denote the experimental data, bars are errors, line is a least square fitting with a function of ~ $P^{1/n}$, where n = 3.4; (b) Epiluminescent images of discrete 8T-UCNP-PEI deposited on a coverslip versus the corresponding P_{ex}. Scale bar is 1 μm.

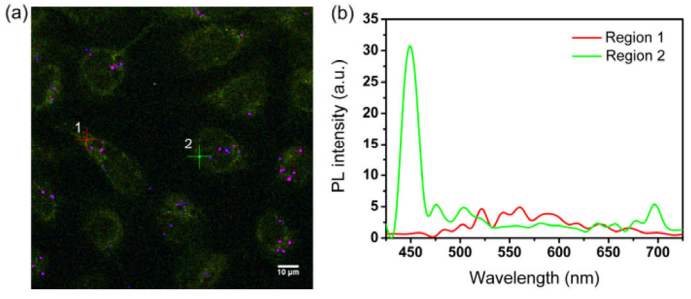

Figure 6 (a) Images of SK-BR-3 cells incubated with 8T-UCNP-PEIs obtained in the Lambda mode. Scale bar is 10 μm. (b) PL spectra acquired from regions 1 and 2 in (a).

Figure 6(a) shows two regions: Region 1 is located on the periphery of the SK-BR-3 cell deprived of 8T-UCNP-PEIs; region 2 contains 8T-UCNP-PEIs. Figure 6(b) shows the corresponding PL spectra of these regions with apparent overlapping. Most of discrete 8T-UCNP-PEIs were observable and interpreted as small clusters engulfed in the endosome/lysosome of cells, while several particles are shadowed by SK-BR-3 cell autofluorescence. This urged us to complement the spectral filtering with temporal filtering.

The temporal filtering approach was based on postprocessing the acquired PL signal time trajectory captured by TCSPC to make use $\tau_{UC} \gg \tau_{af}$ (τ_{af} is the autofluorescence lifetime). As schematically shown in Fig. 7, the main idea of this approach was to clear TCSPC time bins in a time interval t_{clear} corresponding to the autofluorescence emission occurring during τ_{af} after an excitation fs-pulse. The remaining signal in (t_{cycle} – t_{clear}) TCSPC time interval was believed to contain predominantly PL signals of 8T-UCNP-PEIs. Note that

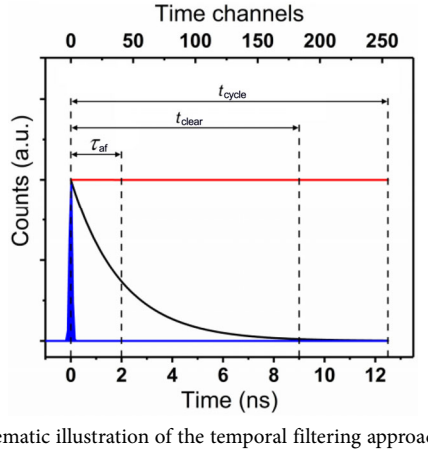

Figure 7 Schematic illustration of the temporal filtering approach. Blue, black, and red lines represent time trajectories of a laser pulse, autofluorescence, and PL of 8T-UCNP, respectively.

the blurring effect was eliminated due to $\tau_{UC} \ll t_{dw}$, although the fast almost artifact-free laser-scanning imaging of UCNPs was demonstrated at t_{dw} = 12.5 μs comparable to τ_{UC} [34].

The contrast of several 8T-UCNP-PEI images at variable t_{clear} was measured and optimized as follows. First, we obtained the mask images of PL 8T-UCNP-PEI at t_{clear} = 9.8 ns. Then, a 10% level of the maximal intensity in the image was taken as a threshold value cutting off PL of the 8T-UCNP-PEI from the autofluorescence of the cells. Inverted masks for PL 8T-UCNP-PEI were used as background masks. Contrast (C) was calculated using the following formula:

$$C = \frac{\overline{UC} - \overline{BG}}{\overline{BG}} \quad (6)$$

where $\overline{UC}$ is the average value of the PL signal of the 8T-UCNP-PEI, and $\overline{BG}$ is the average value of the background signal consisting of the autofluorescence signal and the detector noise. Figure 8 shows images of SK-BR-3 cells incubated with 8T-UCNP-PEI obtained at t_{clear} = 0 and 9.8 ns.

As a result, the average contrast was increased > 2.5 times from 35 to 88, as calculated from the raw and processed image, respectively.

To confirm the detection of single 8T-UCNP-PEIs or small clusters, epiluminescent and AFM images of 8T-UCNP-PEIs deposited on a coverslip were acquired and presented in Fig. 9. To find the same image areas, the coverslip was marked with a diamond glass cutter.

An analysis of the obtained data showed that the height of nanoparticles labeled as 1, 2, and 3 in Figs. 9(a) and 9(b) did not exceed 40 nm (Fig. 9(c)), which agreed with the average diameter of single 8T-UCNP-PEIs as determined by TEM. At the same time, the object to the right of particle 3 in the AFM image (Fig. 9(a), marked by a white arrow) was noticeable in the epiluminescent image (Fig. 9(b)) and was attributed to debris on the cover slip. AFM is characterised by the sub-nanometer axial resolution, whereas its lateral resolution represents a convolution of the object actual size with the tip diameter and can be much coarser. This means that although UCNPs look similar in the image of Fig. 9, their actual diameters most likely differed and their photoluminescent signals varied.

A histogram of the PL intensity distribution of 8T-UCNP-PEIs deposited on a cover slip was plotted to determine the particle-size distribution (PSD), as shown in Fig. 10. The obtained PSD was fitted with a single Gaussian function (Fig. 10(a)) and indicated

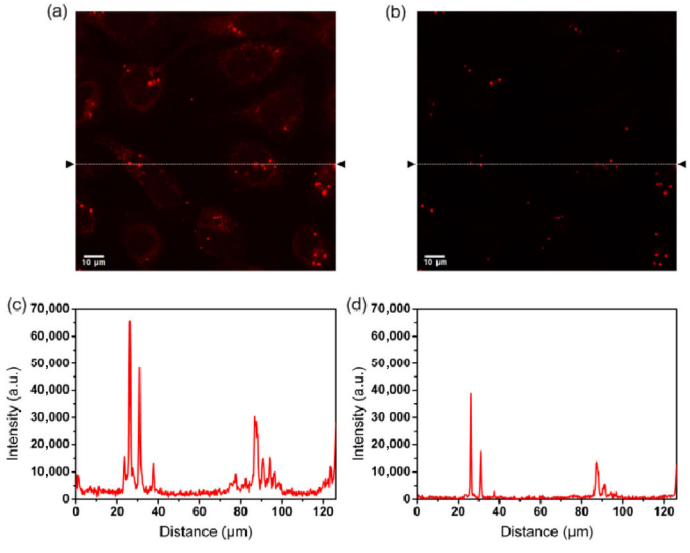

Figure 8 Images of SK-BR-3 cells incubated with 8T-UCNP-PEIs obtained (a) without and (b) with the temporal filtering. Image profiles are plotted along straight lines between points marked by arrows on (a) and (b) for modes (c) without and (d) with delayed detection of PL, respectively.

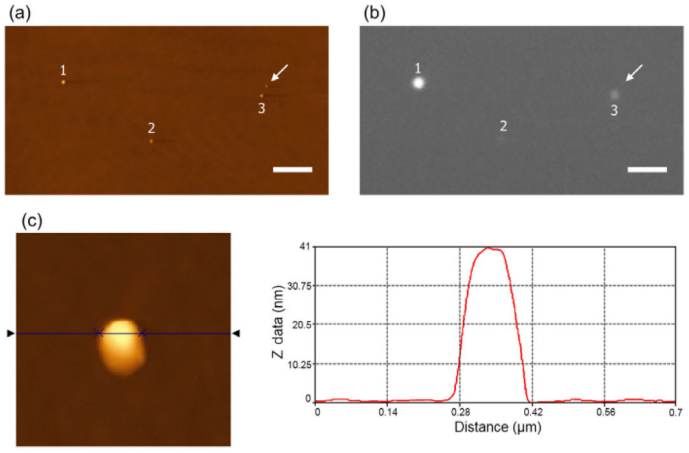

Figure 9 Images of 8T-UCNP-PEI on cover glass obtained by (a) AFM and (b) laser-scanning MPM. Scale bar is 1 μm. (c) Zoomed-in image and corresponding profile of a particle marked 3 on (a).

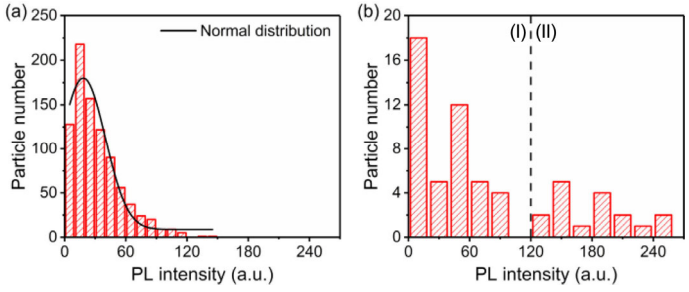

Figure 10 PL intensity distribution of 8T-UCNP-PEIs located (a) on cover slip and (b) in SK-BR-3 cell culture.

monodisperse PSD of the tested colloidal solution. The PL intensity distribution of the images of 8T-UCNP-PEIs incubated with SK-BR-3 cells was apparently polydisperse.

Two specific regions denoted as (I) and (II) were distinct, as shown in Fig. 10(b). The PSD in region (I) (Fig. 10(b)) conformed the PSD in Fig. 10(a) and lent a straightforward interpretation of single or small cluster 8T-UCNP-PEIs present in the intra- and extra-cellular spaces. The PSD in region (II) pointed to the larger-size 8T-UCNP-PEI aggregates. The aggregate formation in the culture medium and cells was not surprising. Strong electrostatic repulsion of 8T-UCNP-PEIs in water due to the large positive surface charge [41] was screened in the saline solution of the culture medium and probably prompted the aggregation. The intracellular aggregation could be explained by the endosome-mediated nanoparticle internalization, where several nanoparticles were enclosed in a single endosome leading to their aggregation.

We also studied the applicability of the proposed approach when imaging 8T-UCNP-PEIs in a complex biological environment, such as tissue of small animals. To this aim, we injected 150 μL of 8T-UCNP-PEI (200 μg/mL) intravenously to Balb/c mice. The animal organs, including spleen, were harvested 15 min post-injection, tissue-sliced and subjected to microscopic examination. Hepatic (80%–85%) and splenic macrophages (10%–15%) are known to be mainly responsible for cleaning the blood flow from the injected colloid. Thus, 8T-UCNP-PEI accumulation was expected in the spleen tissues to demonstrate the proposed approach. Figure 11 shows images of the spleen incubated with 8T-UCNP-PEIs obtained in modes without (Fig. 11(a)) and with (Fig. 11(b)) the temporal filtering.

To confirm the imaging of the 8T-UCNP-PEI, the images were also obtained in the Lambda mode (Fig. 11(c). Figure 11(d) shows the image profiles without (in black) and with (in elimination of the background signal) by cleaning the time window t_{clear} = 9.0 ns after a laser pulse can be seen in the figure. The contrast calculation for

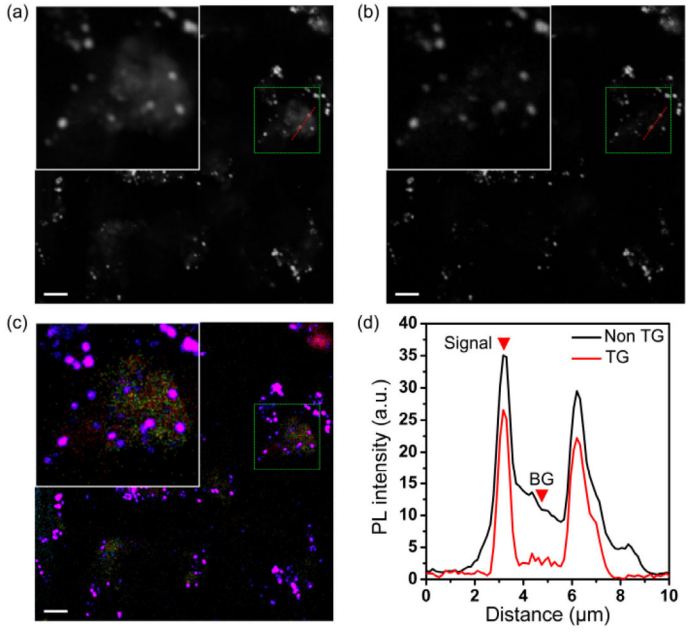

Figure 11 Images of spleen tissue cross-section 15 min post intravascular injection of 8T-UCNP-PEI formulation obtained (a) without and (b) with temporal filtering, respectively. (c) Image of spleen slice obtained in the Lambda mode. (d) Profiles of images without (non TG, in black) and with (TG, in red) delayed detection along red dotted lines on (a) and (b). Signal and BG denote PL signal of 8T-UCNP-PEI and background signal due to spleen tissue autofluorescence, respectively.

the points marked by the red arrows in Figs. 11(a) and 11(b) showed that the achieved contrast enhancement was > 3.5 by implementing the image postprocessing.

4 Conclusions

Due to their high optical nonlinearity as observed experimentally and described theoretically, amplified stimulated emission of 8T-UCNPs enabled imaging of discrete upconversion nanoparticles against a background of cell autofluorescence in laser-scanning MPM coupled to a time-correlated single photon counting module. The enhanced (> 2.5-fold for cells and > 3.5-fold for tissues) 8T-UCNP visibility was also achieved by suppressing the autofluorescence background at the postprocessing stage via clearing the TCSPC time bins corresponding to the fast-decaying autofluorescence while the persistent emission from UCNPs became the main contributor to the recorded signal. The demonstrated method is believed to be suitable for high-contrast imaging of phosphorescence nanomaterials, such as 8T-UCNP, in biological systems by using commercially available laser-scanning nonlinear microscopy.

Acknowledgements

This work was supported by the Russian Foundation for Basic Research (No. 18-29-01055). The high-resolution imaging was carried out with the support of the Russian Foundation for Basic Research (No. 18-34-00723).

References

[1] Pradère, B.; Poulon, F.; Compérat, E.; Lucas, I. T.; Bazin, D.; Doizi, S.; Cussenot, O.; Traxer, O.; Abi Haidar, D. Two-photon optical imaging, spectral and fluorescence lifetime analysis to discriminate urothelial carcinoma grades. *J. Biophotonics* **2018**, *11*, e201800065.

[2] Füger, P.; Hefendehl, J. K.; Veeraraghavalu, K.; Wendeln, A. C.; Schlosser, C.; Obermüller, U.; Wegenast-Braun, B. M.; Neher, J. J.; Martus, P.; Kohsaka, S. et al. Microglia turnover with aging and in an Alzheimer's model via long-term *in vivo* single-cell imaging. *Nat. Neurosci.* **2017**, *20*, 1371–1376.

[3] Chen, C. P.; Liang, Z. Y.; Zhou, B.; Li, X. S.; Liu, C.; Ip, N. Y.; Ou, J. Y. *In vivo* near-infrared two-photon imaging of amyloid plaques in deep brain of Alzheimer's disease mouse model. *ACS Chem. Neurosci.* **2018**, *9*, 3128–3136.

[4] Wang, Y. L.; Chen, M.; Alifu, N.; Li, S. W.; Qin, W.; Qin, A. J.; Tang, Z.; Qian, J. Aggregation-induced emission luminogen with deep-red emission for through-skull three-photon fluorescence imaging of mouse. *ACS Nano* **2017**, *11*, 10452–10461.

[5] Grebenik, E. A.; Nadort, A.; Generalova, A. N.; Nechaev, A. V.; Sreenivasan, V. K. A.; Khaydukov, E. V.; Semchishen, V. A.; Popov, A. P.; Sokolov, V. I.; Akhmanov, A. S. et al. Feasibility study of the optical imaging of a breast cancer lesion labeled with upconversion nanoparticle biocomplexes. *J. Biomed. Opt.* **2013**, *18*, 076004.

[6] Hell, S. W.; Bahlmann, K.; Schrader, M.; Soini, A.; Malak, H. M.; Gryczynski, I.; Lakowicz, J. R. Three-photon excitation in fluorescence microscopy. *J. Biomed. Opt.* **1996**, *1*, 71–74.

[7] Chen, C. H.; Wang, F.; Wen, S. H.; Su, Q. P.; Wu, M. C. L.; Liu, Y. T.; Wang, B. M.; Li, D.; Shan, X. C.; Kianinia, M. et al. Multi-photon near-infrared emission saturation nanoscopy using upconversion nanoparticles. *Nat. Commun.* **2018**, *9*, 3290.

[8] Balu, M.; Baldacchini, T.; Carter, J. L.; Krasieva, T. B.; Zadoyan, R.; Tromberg, B. J. Effect of excitation wavelength on penetration depth in nonlinear optical microscopy of turbid media. *J. Biomed. Opt.* **2009**, *14*, 010508.

[9] Zipfel, W. R.; Williams, R. M.; Webb, W. W. Nonlinear magic: Multiphoton microscopy in the biosciences. *Nat. Biotechnol.* **2003**, *21*, 1369–1377.

[10] Lecoq, J.; Parpaleix, A.; Roussakis, E.; Ducros, M.; Goulam Houssen, Y.; Vinogradov, S. A.; Charpak, S. Simultaneous two-photon imaging of oxygen and blood flow in deep cerebral vessels. *Nat. Med.* **2011**, *17*, 893–898.

[11] Maiti, S.; Shear, J. B.; Williams, R. M.; Zipfel, W. R.; Webb, W. W. Measuring serotonin distribution in live cells with three-photon excitation. *Science* **1997**, *275*, 530–532.

[12] LaComb, R.; Nadiarnykh, O.; Campagnola, P. J. Quantitative second harmonic generation imaging of the diseased state osteogenesis imperfecta: Experiment and simulation. *Biophys. J.* **2008**, *94*, 4504–4514.

[13] Débarre, D.; Supatto, W.; Pena, A. M.; Fabre, A.; Tordjmann, T.; Combettes, L.; Schanne-Klein, M. C.; Beaurepaire, E. Imaging lipid bodies in cells and tissues using third-harmonic generation microscopy. *Nat. Methods* **2006**, *3*, 47–53.

[14] Zhou, L.; Wang, R.; Yao, C.; Li, X. M.; Wang, C. L.; Zhang, X. Y.; Xu, C. J.; Zeng, A. J.; Zhao, D. Y.; Zhang, F. Single-band upconversion nanoprobes for multiplexed simultaneous *in situ* molecular mapping of cancer biomarkers. *Nat. Commun.* **2015**, *6*, 6938.

[15] Hodak, J.; Chen, Z. J.; Wu, S.; Etchenique, R. Multiphoton excitation of upconverting nanoparticles in pulsed regime. *Anal. Chem.* **2016**, *88*, 1468–1475.

[16] Liu, Y. J.; Lu, Y. Q.; Yang, X. S.; Zheng, X. L.; Wen, S. H.; Wang, F.; Vidal, X.; Zhao, J. B.; Liu, D. M.; Zhou, Z. G. et al. Amplified stimulated emission in upconversion nanoparticles for super-resolution nanoscopy. *Nature* **2017**, *543*, 229–233.

[17] Wang, G. F.; Qin, W. P.; Wang, L. L.; Wei, G. D.; Zhu, P. F.; Kim, R. Intense ultraviolet upconversion luminescence from hexagonal $NaYF_4$:Yb^{3+}/Tm^{3+} microcrystals. *Opt. Express* **2008**, *16*, 11907–11914.

[18] Khaydukov, E. V.; Mironova, K. E.; Semchishen, V. A.; Generalova, A. N.; Nechaev, A. V.; Khochenkov, D. A.; Stepanova, E. V.; Lebedev, O. I.; Zvyagin, A. V.; Deyev, S. M. et al. Riboflavin photoactivation by upconversion nanoparticles for cancer treatment. *Sci. Rep.* **2016**, *6*, 35103.

[19] Yu, J. H.; Kwon, S. H.; Petrášek, Z.; Park, O. K.; Jun, S. W.; Shin, K.; Choi, M.; Park, Y. I.; Park, K.; Na, H. B. et al. High-resolution three-photon biomedical imaging using doped ZnS nanocrystals. *Nat. Mater.* **2013**, *12*, 359–366.

[20] Peng, X. Y.; Huang, B. R.; Pu, R.; Liu, H. C.; Zhang, T.; Widengren, J.; Zhan, Q. Q.; Ågren, H. Fast upconversion super-resolution microscopy with 10 μs per pixel dwell times. *Nanoscale* **2019**, *11*, 1563–1569.

[21] Yu, M. X.; Li, F. Y.; Chen, Z. G.; Hu, H.; Zhan, C.; Yang, H.; Huang, C. H. Laser scanning up-conversion luminescence microscopy for imaging cells labeled with rare-earth nanophosphors. *Anal. Chem.* **2009**, *81*, 930–935.

[22] Song, Z.; Anissimov, Y. G.; Zhao, J. B.; Nechaev, A. V.; Nadort, A.; Jin, D. Y.; Prow, T. W.; Roberts, M. S.; Zvyagin, A. V. Background free imaging of upconversion nanoparticle distribution in human skin. *J. Biomed. Opt.*

2013, *18*, 061215.

[23] Park, Y. I.; Kim, H. M.; Kim, J. H.; Moon, K. C.; Yoo, B.; Lee, K. T.; Lee, N.; Choi, Y.; Park, W.; Ling, D. S. et al. Theranostic probe based on lanthanide-doped nanoparticles for simultaneous *in vivo* dual-modal imaging and photodynamic therapy. *Adv*. *Mater*. **2012**, *24*, 5755–5761.

[24] Li, H.; Wang, L. Y. Preparation and upconversion luminescence cell imaging of o-carboxymethyl chitosan-functionalized $NaYF_4$:Yb^{3+}/Tm^{3+}/Er^{3+} nanoparticles. *Chin*. *Sci*. *Bull*. **2013**, *58*, 4051–4056.

[25] Zijlmans, H. J. M. A. A.; Bonnet, J.; Burton, J.; Kardos, K.; Vail, T.; Niedbala, R. S.; Tanke, H. J. Detection of cell and tissue surface antigens using up-converting phosphors: A new reporter technology. *Anal*. *Biochem*. **1999**, *267*, 30–36.

[26] Guller, A. E.; Generalova, A. N.; Petersen, E. V.; Nechaev, A. V.; Trusova, I. A.; Landyshev, N. N.; Nadort, A.; Grebenik, E. A.; Deyev, S. M.; Shekhter, A. B. et al. Cytotoxicity and non-specific cellular uptake of bare and surface-modified upconversion nanoparticles in human skin cells. *Nano Res*. **2015**, *8*, 1546–1562.

[27] Guryev, E. L.; Shilyagina, N. Y.; Kostyuk, A. B.; Sencha, L. M.; Balalaeva, I. V.; Vodeneev, V. A.; Kutova, O. M.; Lyubeshkin, A. V.; Yakubovskaya, R. I.; Pankratov, A. A. et al. Preclinical study of biofunctional polymer-coated upconversion nanoparticles. *Toxicol*. *Sci*. **2019**, *170*, 123–132.

[28] Suyver, J. F.; Grimm, J.; Van Veen, M. K.; Biner, D.; Krämer, K. W.; Güdel, H. U. Upconversion spectroscopy and properties of $NaYF_4$ doped with Er^{3+}, Tm^{3+} and/or Yb^{3+}. *J*. *Lumin*. **2006**, *117*, 1–12.

[29] Fan, Y.; Wang, P. Y.; Lu, Y. P.; Wang, R.; Zhou, L.; Zheng, X. L.; Li, X. M.; Piper, J. A.; Zhang, F. Lifetime-engineered NIR-II nanoparticles unlock multiplexed *in vivo* imaging. *Nat*. *Nanotechnol*. **2018**, *13*, 941–946.

[30] Razali, W. A.; Sreenivasan, V. K. A.; Bradac, C.; Connor, M.; Goldys, E. M.; Zvyagin, A. V. Wide-field time-gated photoluminescence microscopy for fast ultrahigh-sensitivity imaging of photoluminescent probes. *J*. *Biophotonics* **2016**, *9*, 848–858.

[31] Tu, C. C.; Awasthi, K.; Chen, K. P.; Lin, C. H.; Hamada, M.; Ohta, N.; Li, Y. K. Time-gated imaging on live cancer cells using silicon quantum dot nanoparticles with long-lived fluorescence. *ACS Photonics* **2017**, *4*, 1306–1315.

[32] Nadort, A.; Sreenivasan, V. K. A.; Song, Z.; Grebenik, E. A.; Nechaev, A. V.; Semchishen, V. A.; Panchenko, V. Y.; Zvyagin, A. V. Quantitative imaging of single upconversion nanoparticles in biological tissue. *PLoS One* **2013**, *8*, e63292.

[33] Wu, S. W.; Han, G.; Milliron, D. J.; Aloni S, Altoe, V.; Talapin, D. V.; Cohen, B. E.; Schuck, P. J. Non-blinking and photostable upconverted luminescence from single lanthanide-doped nanocrystals. *Proc*. *Natl*. *Acad*. *Sci*. *USA* **2009**, *106*, 10917–10921.

[34] Lu, Y. Q.; Zhao, J. B.; Zhang, R.; Liu, Y. J.; Liu, D. M.; Goldys, E. M.; Yang, X. S.; Xi, P.; Sunna, A.; Lu, J. et al. Tunable lifetime multiplexing using luminescent nanocrystals. *Nat*. *Photonics* **2014**, *8*, 32–36.

[35] Liu, J.; Li, N. N.; Wu, R. T.; Zhao, Y. X.; Zhan, Q. Q.; He, S. L. Sub-5-nm lanthanide-doped ZrO_2@$NaYF_4$ nanodots as efficient upconverting probes for rapid scanning microscopy and aptamer-mediated bioimaging. *Opt*. *Mater*. *Express* **2015**, *5*, 1759–1771.

[36] Ding, M. Y.; Chen, D. Q.; Ma, D. Y.; Liu, P.; Song, K. X.; Lu, H. W.; Ji, Z. G. Tuning the upconversion luminescence lifetimes of KYb_2F_7:Ho^{3+} nanocrystals for optical multiplexing. *ChemPhysChem* **2015**, *16*, 3784–3789.

[37] Zhao, J. B.; Jin, D. Y.; Schartner, E. P.; Lu, Y. Q.; Liu, Y. J.; Zvyagin, A. V.; Zhang, L. X.; Dawes, J. M.; Xi, P.; Piper, J. A. et al. Single-nanocrystal sensitivity achieved by enhanced upconversion luminescence. *Nat*. *Nanotechnol*. **2013**, *8*, 729–734.

[38] Joubert, M. F.; Guy, S.; Jacquier, B. Model of the photon-avalanche effect. *Phys*. *Rev*. *B* **1993**, *48*, 10031–10037.

[39] Auzel, F.; Chen, Y. H. Photon avalanche luminescence of Er^{3+} ions in $LiYF_4$ crystal. *J*. *Lumin*. **1995**, *65*, 45–56.

[40] Pelle, G. F. Photon avalanche fluorescence and lasers. *Opt*. *Mater*. **1996**, *5*, 239–249.

[41] Guller, A. E.; Nadort, A.; Generalova, A. N.; Khaydukov, E. V.; Nechaev, A. V.; Kornienko, I. A.; Petersen, E. V.; Liang, L. E.; Shekhter, A. B.; Qian, Y. et al. Rational surface design of upconversion nanoparticles with polyethylenimine coating for biomedical applications: Better safe than brighter? *ACS Biomater*. *Sci*. *Eng*. **2018**, *4*, 3143–3153.

[42] Bradac, C.; Johnsson, M. T.; Breugel, M. V.; Baragiola, B. Q.; Martin, R.; Juan, M. L.; Brennen, G. K.; Volz, T. Room-temperature spontaneous superradiance from single diamond nanocrystals. *Nat*. *Commun*. **2017**, *8*, 1205.